OPTICS

Four-wave mixing of topological edge plasmons in graphene metasurfaces

Jian Wei You, Zhihao Lan, Nicolae C. Panoiu*

We study topologically protected four-wave mixing (FWM) interactions in a plasmonic metasurface consisting of a periodic array of nanoholes in a graphene sheet, which exhibits a wide topological bandgap at terahertz frequencies upon the breaking of time reversal symmetry by a static magnetic field. We demonstrate that due to the significant nonlinearity enhancement and large life time of graphene plasmons in specific configurations, a net gain of FWM interaction of plasmonic edge states located in the topological bandgap can be achieved with a pump power of less than 10 nW. In particular, we find that the effective nonlinear edge-waveguide coefficient is about $\gamma \simeq 1.1 \times 10^{13}$ W^{-1} m^{-1}, i.e., more than 10 orders of magnitude larger than that of commonly used, highly nonlinear silicon photonic nanowires. These findings could pave a new way for developing ultralow-power-consumption, highly integrated, and robust active photonic systems at deep-subwavelength scale for applications in quantum communications and information processing.

INTRODUCTION

In the past decade, topological photonics has emerged as a rapidly burgeoning field of exploration of topological physics ideas framed in the context of photonics. This area of research began with the theoretical work by Haldane and Raghu (1, 2), where they constructed an analog of quantum Hall edge states in photonic crystals based on magneto-optical media and observed topological edge modes within the corresponding photonic bandgaps. Shortly afterward, an experimental realization and observation of such topological edge modes in a magneto-optical photonic crystal were reported in the microwave regime (3). Since then, there has been increasing interest in implementing in photonics topological states of matter and developing new ideas specific to topological photonics (4–8).

In addition to new perspectives brought in fundamental science, topological photonics also offers a broad array of potential applications for novel photonic devices, as its exotic features have already prompted the reexamination of some traditional views on light manipulation and propagation. For instance, reducing back reflection is a major challenge in optical waveguides, and in this context, the unidirectional topological waveguide (9–11) is an ideal light transport device in integrated photonics, as it could transmit light without backscattering even in the presence of inherent structural disorder. Moreover, some new concepts of topological photonics have also led to the development of novel photonic devices, such as optical isolators (12, 13), robust delay lines (14, 15), signal switches (16), nonreciprocal devices (17–19), and topological lasers (20, 21).

Most of the previous studies have focused on linear topological photonic systems; however, topological physics could also play an important role in the nonlinear regime, leading to previously unknown collective phenomena and strongly correlated states of light (8, 22–24). For instance, a topological source of quantum light has recently been realized in a nonlinear photonic system, which paves a new way for the development of robust quantum photonic devices (22). Moreover, a novel and sensitive approach for

imaging topological edge states with third-harmonic generation has been recently demonstrated experimentally (24).

In this work, we demonstrate topologically protected four-wave mixing (FWM) interactions in a graphene metasurface upon the breaking of time reversal symmetry by a static magnetic field. In particular, we show that due to large optical near-field enhancement and large life time of graphene plasmons in such metasurfaces, a net gain of FWM interaction of plasmonic edge states located in the topological bandgap can be achieved at an ultralow pump power of less than 10 nW. This remarkable feature is a direct consequence of the unusually large effective nonlinear edge-waveguide coefficient, $\gamma \simeq 1.1 \times 10^{13}$ W^{-1} m^{-1}, which, to the best of our knowledge, to date is by far the largest reported nonlinear optical coefficient of a light guiding physical system.

RESULTS

The system

We study a topologically protected nonlinear FWM process in a graphene plasmonic system. Graphene distinguishes itself as an ideal platform to study nonlinear topological photonics in several key aspects: First, graphene exhibits large nonlinearity over a broad spectral range, from terahertz to visible light. In particular, it has been shown (25) that graphene in a strong magnetic field has the largest third-order susceptibility of all known materials. Second, some recent studies (26, 27) revealed that topologically protected one-wave edge plasmons can be realized in graphene metasurfaces. In addition to the typical plasmonic effects, such as local field enhancement and field confinement, the local field can be further confined to the edge of the graphene plasmonic system, leading to a marked enhancement of the nonlinear optical response of the graphene system. Third, phase matching is a crucial condition in nonlinear frequency mixing processes. In contrast to the frequently used bulk modes (22), where several modes with different wave vectors usually exist at a given frequency, a topological edge mode with absolute value of the Chern number equal to one, as it is the case with the graphene metasurface investigated in this study, has a unique wave vector at a fixed frequency. Therefore, the phase matching condition can be achieved and implemented experimentally much more easily, as in

Department of Electronic and Electrical Engineering, University College London, Torrington Place, London WC1E 7JE, UK.
*Corresponding author. Email: n.panoiu@ucl.ac.uk

this case only one mode can be excited at a specific frequency. These important features make graphene plasmonic systems particularly appealing in the design of highly integrated nonlinear topological nanophotonic devices.

The nonlinear system explored in this work is illustrated in Fig. 1. A graphene plasmonic metasurface consisting of a periodic nano-hole array with hexagonal symmetry is placed in a static magnetic field. Because of the time reversal symmetry breaking induced by the magneto-optical response of graphene under an external magnetic field, this plasmonic system could have a topological bandgap. After a geometry optimization, the topological bandgap could become wide enough so that it readily accommodates the optical modes taking part in an FWM process. To induce an FWM process, the system is excited by an external source at the pump frequency ω_p, as illustrated in Fig. 1. Because of the strong third-order nonlinearity of graphene, a degenerate FWM process could take place, where two photons in a pump mode will generate a pair of photons at the signal and idler frequencies, ω_s and ω_i, respectively. As a result, the energy of the pump mode (green) in Fig. 1 is transferred to the (seeded) signal (blue) and idler (red) modes, leading to the pump decay and the amplification of the signal and idler. This degenerate FWM process is topologically protected by the chiral nature of the edge plasmons.

Topological bands of the graphene plasmonic system: Linear response

We first study the linear optical response of our graphene plasmonic system by calculating its photonic band structure using a numerical approach based on the finite element method (FEM). The unit cell (with lattice constant a and air hole radius r) and the first Brillouin zone of the system used in our simulations are shown in Fig. 2 (A and B). The band diagrams of the system ($a = 400$ nm, $r = 120$ nm) at different magnetic fields $B = 0, 2, 5, 7, 10$ T are presented in Fig. 2C, where the parameters of the graphene are set to be $E_F = 0.2$ eV, $v_F = 10^6$ ms^{-1}, and $\tau = 50$ ps (see Materials and Methods for details).

There are several notable features of the results presented in Fig. 2C. First, without the external magnetic field ($B = 0$), due to the hexagonal symmetry of the metasurface structure, Dirac cones that are protected by the parity (P) inversion and time reversal (T) symmetries exist at K and K' symmetry points of the Brillouin zone (26). Second, in the presence of the magnetic field ($B \neq 0$), the time reversal symmetry of the system is broken and, consequently, the Dirac cones are gapped out, resulting in a topological nontrivial bandgap. Moreover, the width $\Delta \nu$ of this bandgap increases as the amplitude of the magnetic field increases.

To confirm the topological nature of the bandgap, we illustrate the emergence of the edge modes within the bandgap for a system

that has finite size along the y axis, i.e., the number of unit cells along this direction is finite (chosen to be 20 in our FEM simulations), whereas the system is periodic along the x axis (in the FEM simulations, periodic boundary conditions are imposed at the left and right boundaries along the x axis; see Fig. 3A). The supercell for this finite system is shown by a green rectangle in Fig. 3A, whose width and length are a and $b = \sqrt{3}a$, respectively.
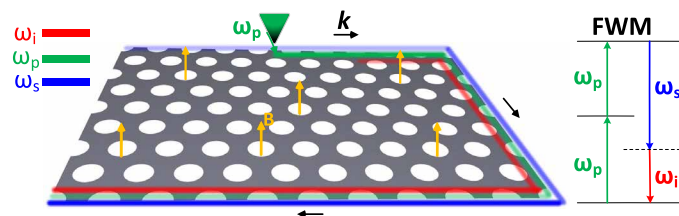
The projected band diagrams along k_x, determined for $B = 0, 2, 5, 7, 10$ T, are depicted in Fig. 3B. First, similar to what we observed in Fig. 2C, a bandgap opens when one applies an external static magnetic field ($B \neq 0$), with the gap width $\Delta \nu$ increasing as the amplitude of magnetic field increases. However, different from the band diagrams of an infinite graphene metasurface shown in Fig. 2C, in the band diagrams of Fig. 3B, there are two additional edge modes at the top (red) and bottom (blue) boundaries of the finite graphene system. These two edge modes connect the bulk bands located above and below the bandgap and cannot be moved out of the bandgap into the bulk bands as long as the bandgap exists. In other words, they are robust and defect immune, which is guaranteed by the topological protection of the bandgap.

One can also calculate the gap Chern number, which is a topological invariant that characterizes the topological properties of the bandgap, to further confirm that the bandgap discussed above is topologically nontrivial and that these edge modes are topological modes (26). To this end, we indicate in Fig. 3B the calculated gap Chern number. Since the gap Chern number is −1 (the magnitude indicates the number of topological edge modes, whereas the sign shows the direction of propagation), there is only one topologically protected edge mode for each edge termination. In other words, our graphene structure supports modes that can exhibit unidirectional and defect-immune propagation features along the top and bottom edges. Moreover, the property of unidirectional propagation of the edge modes is also illustrated by the slope of their frequency dispersion curve, as their group velocity, $v_g = \partial \omega / \partial k$, within the topological bandgap is either positive (top edge) or negative (bottom edge).
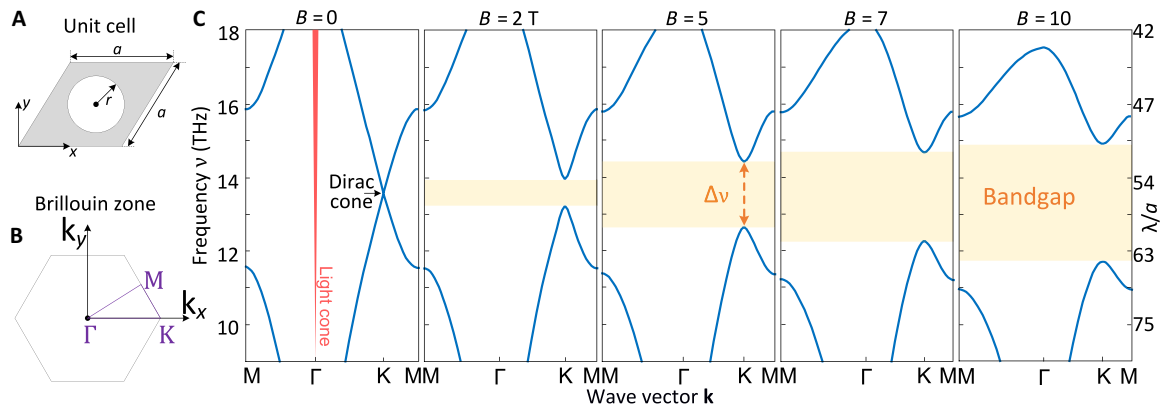
To gain deeper insights into the physical properties of plasmonic bulk and edge modes of the graphene metasurface, the near-field distribution of these modes propagating in a finite graphene plasmonic metasurface (four unit cells along the y axis and about 15 unit cells along the x axis, as per Fig. 4, B and C) is studied by using full-wave FEM simulations. In these computations, a perfectly matched layer is used at the left side of the graphene structure, whereas at the other sides, we imposed scattering boundary conditions so as to mimic infinite air space. To excite this finite graphene system, an electric source ($E_0 = 2 \times 10^4$ V/m) depicted by a red triangle in Fig. 4B is used.

In the case of the bulk mode, we choose the source frequency $V_b = 16$ THz, which belongs to the bulk region (see Fig. 4A). As expected, the corresponding optical field spreads throughout the graphene structure (see Fig. 4B), which proves that bulk modes are excited in this case. It should be noted that, due to the plasmonic characteristics of the graphene bulk modes, their optical field is tightly confined at the surface of the graphene metasurface.
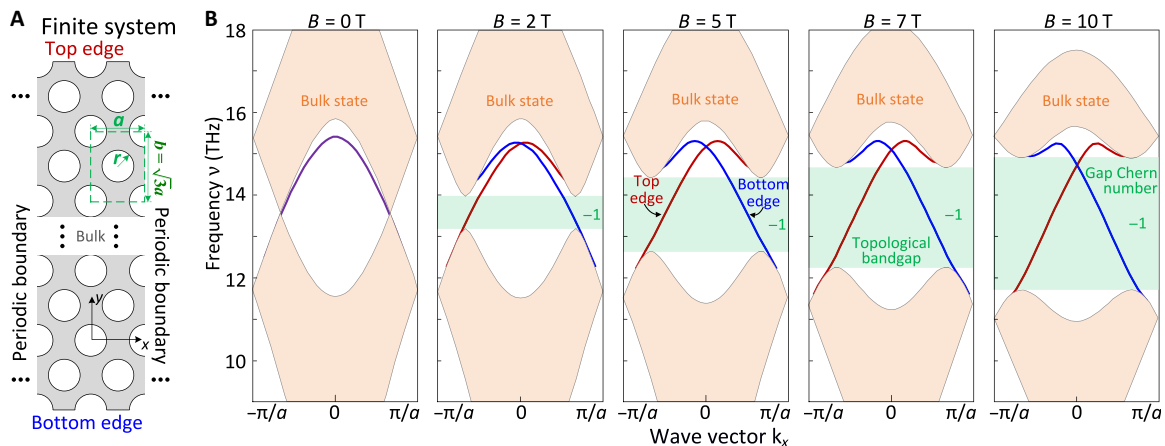
In the case of the excitation of an edge mode, we choose a frequency in the bandgap, $\nu_p = 13.17$ THz, so that at this frequency only the edge mode exists, as per Fig. 4A. The corresponding field profile generated by the source in the finite system, presented in Fig. 4C, illustrates several notable features. Thus, the optical field does not penetrate in the bulk region and only propagates unidirectionally along the edge of the graphene metasurface. In addition,

Fig. 1. FWM of topologically protected one-way edge plasmons in a graphene metasurface consisting of a periodic nanohole array with hexagonal symmetry in a static magnetic field and the corresponding energy level diagram of a degenerate FWM process.

Fig. 2. Band diagrams of the graphene plasmonic metasurface. (**A**) Unit cell and (**B**) the first Brillouin zone of the metasurface. (**C**) Band diagrams of the metasurface at $B = 0, 2, 5, 7, 10$ T. As the Dirac cone is below the air light cone, surface plasmons can exist at deep-subwavelength scale ($\lambda/a > 40$). Moreover, a topological bandgap is opened in the presence of an external static magnetic field.

Fig. 3. Band diagrams of a finite graphene metasurface. (**A**) Geometry of the finite graphene metasurface, where the number of unit cells (green dashed frame) is finite along the y axis and infinite along the x axis. (**B**) Projected band diagrams of the metasurface at $B = 0, 2, 5, 7$, and 10 T, where the edge modes on the top and bottom boundaries are depicted by red and blue curves, respectively. Since the gap Chern number characterizes the number of edge modes in the gap, there is a single edge mode at each boundary.

because of the chiral nature of the edge mode, this unidirectional propagation is robust against structural defects, which allows it to circumvent defects (e.g., sharp bends) without producing backscattering. These features prove that the edge modes within the topological bandgap in Fig. 4A are topologically protected. Last but not least, we note that in addition to the plasmonic field confinement effect illustrated in Fig. 4 (B and C), the optical field of the edge modes is further confined to the edge of the system, which is particularly important when one seeks to enhance nonlinear optical interactions such as FWM.
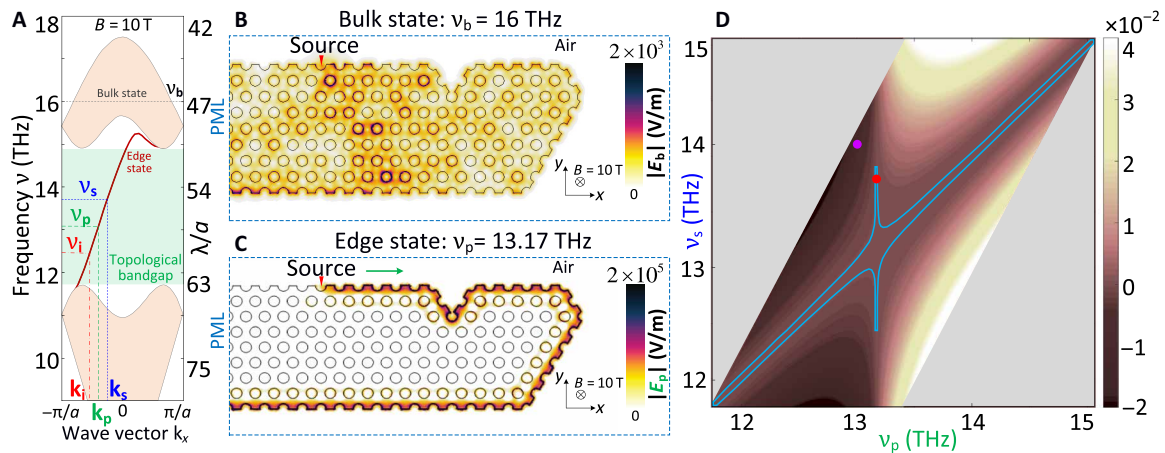
Nonlinear interaction of edge states: FWM

Comparing Fig. 4 (B and C), one can see that, in the case of the edge mode, the plasmon-induced field enhancement effect quantified by the ratio $|E_e|_{max}/E_0$ is two orders of magnitude stronger than that in the case of the bulk mode $|E_b|_{max}/E_0$, namely, $|E_e|_{max}/|E_b|_{max} > 100$. Moreover, the results in Fig. 4A show that at a particular frequency, there is only a single-edge mode, with a unique wave vector, whereas several different bulk modes can be excited at one frequency. The former effect is important in enhancing the nonlinear optical

interactions, whereas the latter one is particularly useful for engineering physical configurations in which phase matching in FWM is achieved.

To illustrate these ideas, in what follows, we analyze the circumstances in which the phase matching condition in a degenerate FWM of one-way edge modes can be fulfilled. To this end, we calculate the normalized wave vector mismatch, defined as $\Delta\kappa \equiv \alpha\Delta k = a(2k_p - k_s - k_i)$, corresponding to an FWM process in which a pump edge mode with wave vector $\mathbf{k}_p$ gives rise to signal and idler edge modes with wave vectors $\mathbf{k}_s$ and $\mathbf{k}_i$, respectively. In particular, the exchange of energy among the interacting waves is most efficient when the phase matching condition $\Delta\kappa = 0$ is satisfied. Unlike the wave vector, the energy is conserved in the FWM process, meaning $2\nu_p = \nu_s + \nu_i$.

Starting from the mode dispersion curves of the topological edge modes presented in Fig. 4A, and using the energy conservation relation that characterizes the FWM process, the corresponding dispersion map of the normalized wave vector mismatch $\Delta\kappa$ is calculated numerically and depicted in Fig. 4D. In particular, for the sake of a better quantitative understanding of the energy conversion efficiency of the FWM process, we also show in this figure the

Fig. 4. Nonlinear edge-mode interaction and FWM within a topological bandgap. (**A**) Band diagram of the graphene metasurface at $B = 10$ T. (**B**) Field profile of a bulk mode excitation at $\nu_b = 16$ THz, showing that the optical field spreads throughout the bulk region. (**C**) Field profile of an edge mode excitation at $\nu_b = 13.17$ THz, illustrating its unidirectional and defect-immune propagation along the system edge ($\tau \to \infty$). (**D**) Dispersion map of the normalized wave vector mismatch $\Delta\kappa$. The blue contour is defined by the condition $\Delta\kappa = 10^{-5}$, whereas the red and magenta dots correspond to a nearly phase-matched ($\Delta\kappa = 5.16 \times 10^{-6}$) and a phase-mismatched ($\Delta\kappa = 1.75 \times 10^{-2}$) FWM process, respectively.

contour defined by $\Delta\kappa = 10^{-5}$. More specifically, for frequencies inside the domain defined by this contour, energy is transferred from the pump to the signal and idler over a distance of about $10^5\pi$ lattice constants.

To validate the conclusions derived from the dispersion map of $\Delta\kappa$, we performed full-wave simulations of the nonlinear dynamics of the interacting edge modes. To this end, we chose a point indicated with a red dot in Fig. 4D, characterized by $\nu_p = 13.17$ THz, $\nu_s = 13.72$ THz, and $\nu_i = 12.62$ THz, and for which the FWM interaction is nearly phase matched ($\Delta\kappa = 5.16 \times 10^{-6}$). Moreover, we considered a seeded FWM process in which the input intensity of the signal is much smaller than that of the pump, whereas the input intensity of the idler is set to zero. Specifically, in our FEM simulations, we set the source input field amplitudes at the three frequencies $|E_p| = 2 \times 10^4$ V m^{-1}, $|E_s| = 4 \times 10^2$ V m^{-1}, and $|E_i| = 0$. Last, the nonlinearity of graphene under the influence of a magnetic field of 10 T is described by a third-order susceptibility with value of $\chi^{(3)} = 5 \times 10^{-10}$ m^2 V^{-2} (*25*).

Using the procedure we just described, we have computed the near-field profiles at the frequencies of the pump, signal, and idler, the results of these simulations being summarized in Fig. 5. In these calculations, graphene losses are neglected by setting $\tau \to \infty$. It can be seen in Fig. 5 (A and B) that, as a result of the nonlinear FWM interaction, the signal is amplified upon propagation, whereas an edge mode is generated at the idler frequency (note that in Fig. 5B, there is no external source at the idler frequency). Since the frequency of all the interacting edge modes is located in the topological bandgap, both signal and idler modes are topologically protected and exhibit unidirectional and defect-immune propagation along the system edge.

The FWM process can be further quantitatively investigated by calculating the dependence on the propagation distance of the power carried by the three edge modes. The mode power is calculated by integrating the corresponding Poynting vector across the transverse section of the mode. The results of these calculations are summarized in Fig. 5 (C and D) and correspond to the case of near phase matching discussed above and a case when the FWM process is not phase matched. In the latter case, the system parameters are $\nu_p = 13.03$ THz,
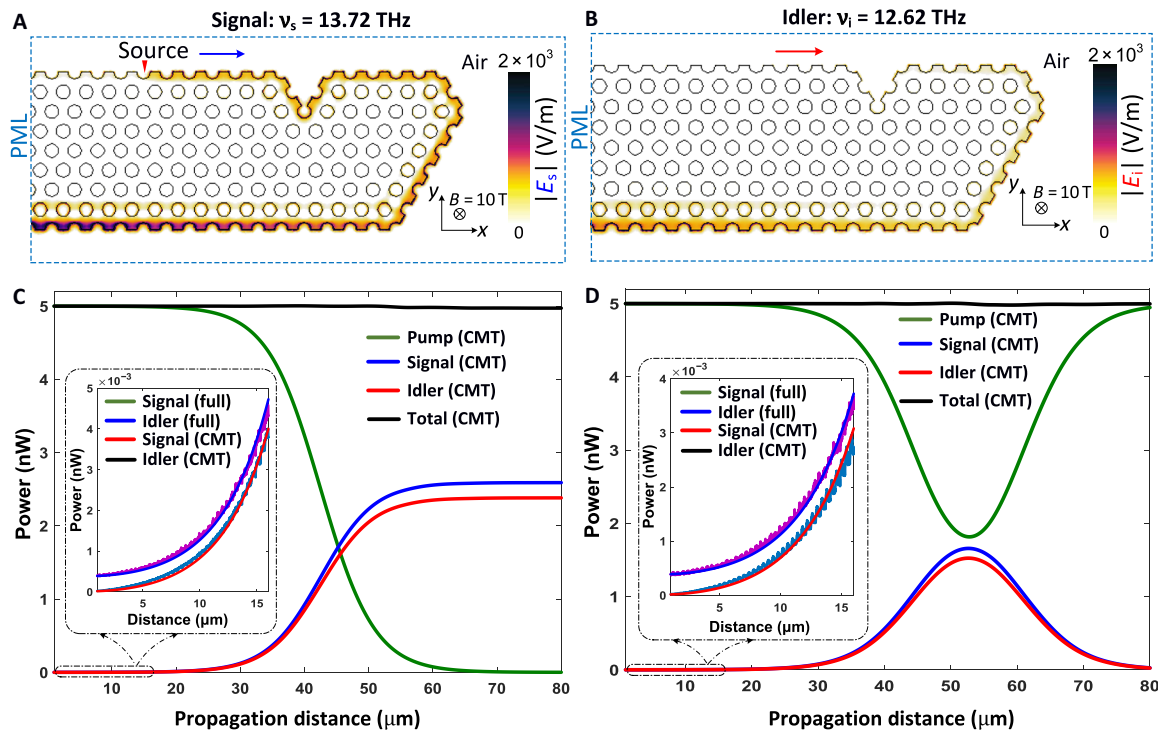
$\nu_s = 14.05$ THz, $\nu_i = 12.01$ THz, and $\Delta\kappa = 1.75 \times 10^{-2}$ (magenta point in Fig. 4D).

There are several important ideas revealed by the results presented in Fig. 5 (C and D). First, the power of both the signal and idler modes is amplified upon propagation, due to the energy conversion from the pump mode. Second, the growth rate of the signal and idler modes in the case of the nearly phase-matched FWM is larger than when the FWM interaction is not phase matched, which means that the energy conversion is more efficient in the former case. Third, the plots presented in the insets of Fig. 5 (C and D) show that the predictions of the coupled-mode theory (CMT), see the Supplementary Materials for details, agree very well with the rigorous results obtained using full-wave simulations of the nonlinear mode interaction, despite the fact that the optical fields at the three frequencies are strongly confined at deep-subwavelength scale and significantly enhanced. This is particularly important in practice because the CMT calculations are much faster and require a much smaller amount of memory as compared with using full-wave simulations.

Our CMT predicts that the effective nonlinear FWM coefficient is $\gamma_{FWM} \approx 2.4 \times 10^{13}$ W^{-1} m^{-1} (see the Supplementary Materials), which is more than 10 orders of magnitude larger than that of silicon photonic wire waveguides (*28*, *29*) and 5 orders of magnitude larger than that of a graphene nanoribbon waveguide (*30*). To the best of our knowledge, to date, this is the largest nonlinear FWM coefficient reported in a nonlinear optical system. This remarkable result is a consequence of the particularly large third-order susceptibility of graphene, which is further enhanced by the plasmon-induced enhancement and extreme confinement of the optical field of the edge modes. In particular, the size of the unit cell of the graphene metasurface is much smaller than the operating wavelength, namely, $\lambda/a > 50$ in our FWM process, a notable feature that can facilitate the design of low-power, ultracompact active photonic nanodevices.

The radiation loss of the edge modes of the graphene metasurface can be neglected because, as we just discussed, they are strongly confined. The intrinsic loss, however, has to be taken into account in practical applications. To study its influence on the FWM interaction, a finite plasmon life time τ is considered in Eqs. 2 and 3.

Fig. 5. Topologically protected FWM process in a graphene metasurface. (**A**) Field profile at the signal frequency, v_s = 13.72 THz. (**B**) Field profile at the idler frequency, v_i = 16.62 THz. (**C**) Dependence on the propagation distance of the mode power of the pump, signal, and idler corresponding to the field profiles shown in (A) and (B), determined using the CMT when the FWM process is phase matched. Also shown in the insets are the same mode powers determined using the CMT and full-wave simulations. The black curve corresponds to the total power and shows that the energy is conserved in the FWM interaction. (**D**) The same as in (C), but corresponding to a case when the FWM interaction is not phase matched.

Similar to the lossless case, we determined the dependence of the power of the interacting edge modes on the propagation distance; the corresponding results of this analysis are presented in Fig. 6.
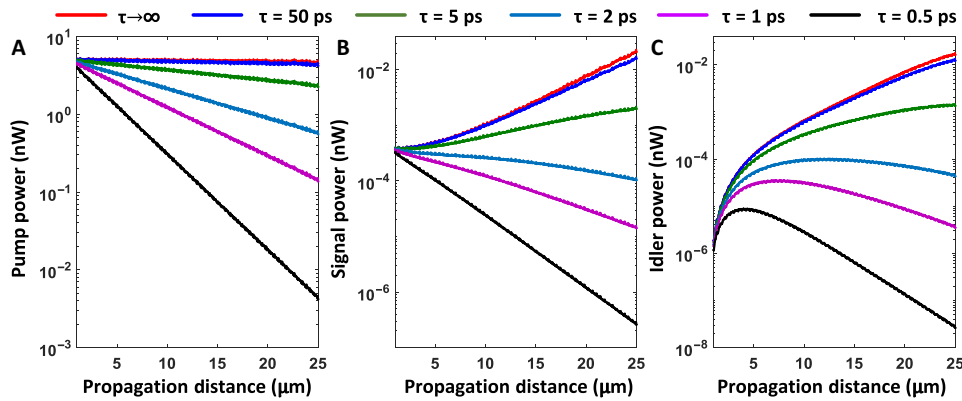
Typically, the plasmon lifetime is determined by the plasmon-phonon coupling and varies from 0.1 to 1 ps (*31*). This loss can be reduced if exfoliated graphene is placed onto a boron nitride substrate (*32*), which leads to a lifetime as large as 3 ps. Moreover, recent experiments (*33*, *34*) have demonstrated that an external magnetic field can also strongly increase the plasmon lifetime, as in this case the two-dimensional surface plasmon can be effectively transformed into a one-dimensional–like edge plasmon. Specifically, it has been shown that by applying an external magnetic field, the plasmon lifetime can be readily increased to 50 ps (*34*).

One remarkable conclusion of the analysis of the FWM interaction of edge modes of our lossy graphene metasurface is that net signal gain can be achieved if the lifetime $\tau \gtrsim 2.5$ ps. This is the first plasmonic system in which net gain can be achieved without incorporating gain optical media in the system. It can be seen in Fig. 6 that whereas the pump decays for all values of the plasmon lifetime, due to the combined contributions of the graphene loss and energy transfer mediated by the FWM interaction, the signal power increases monotonously if $\tau \gtrsim 2.5$ ps. The idler, on the other hand, shows a more complex dynamics. Thus, irrespective of the value of the lifetime, at the beginning of the nonlinear interaction, the power in the idler builds up over a certain distance. After this amplification stage, the power in the idler decays monotonously if $\tau \lesssim 2.5$ ps, because the pump power is no longer large enough to sustain the amplification

of the idler, whereas if $\tau \gtrsim 2.5$ ps, then the power in the idler mode increases monotonously over the entire distance considered in our simulations.

DISCUSSION
Using rigorous full-wave simulations supported by a coupled-mode theory, we have demonstrated a topologically protected nonlinear FWM process in a patterned graphene plasmonic metasurface. In particular, we have shown that a topological bandgap as wide as several terahertz can be created in the metasurface under a strong static magnetic field. Moreover, the analysis of the dispersion properties of the topologically protected edge modes located in the bandgap reveals that FWM interaction is efficiently phase matched in a large domain of the parameter space of the system. Here, we note the dispersion property of edge modes can be engineered by tailoring the edge truncation of the graphene metasurface. The near-field profiles of the interacting edge modes show unidirectional and defect-immune propagation, hence demonstrating that the FWM process is topologically protected. Our study also reveals that, because of an unusually large value of the FWM nonlinear coefficient and the large field enhancement at plasmon resonances, the FWM interaction produces net gain even when plasmon losses in graphene are rigorously taken into account. This notable property of FWM of topological edge modes of graphene metasurfaces might play an important role in the development of new ultracompact and topologically protected active photonic nanodevices.

Fig. 6. Influence of loss on the topologically protected FWM process in graphene metasurface at *B* = 10 T. (A to C) Dependence on the propagation distance of the power of the pump, signal, and idler edge modes, respectively, corresponding to a phase-matched FWM process, determined for different values of the loss rate. Because of the particularly large value of the FWM coefficient, net gain (the FWM gain overcompensates the loss) can be achieved as long as $\tau \gtrsim 2.5$ ps.

MATERIALS AND METHODS

In our modeling of an infinite graphene metasurface, periodic boundary conditions are used for the four edges of the unit cell depicted in Fig. 2A. At infrared and terahertz frequencies, graphene placed in a static magnetic field can be characterized as an electrically gyrotropic material (*35–37*), whose surface conductivity tensor can be represented as

$$\sigma_s = \begin{bmatrix} \sigma_L & \sigma_H \\ -\sigma_H & \sigma_L \end{bmatrix} \tag{1}$$

where the diagonal elements (longitudinal conductivity, σ_L) and the off-diagonal elements (Hall conductivity, σ_H) can be determined using Kubo's formalism (*38*). At room temperature and for frequencies below the visible-light region, the longitudinal and Hall conductivities are given by (*26, 27*)

$$\sigma_L = \sigma_0 \frac{1 - i\omega\tau}{(\omega_c\tau)^2 - (i + \omega\tau)^2} \tag{2}$$

$$\sigma_H = -\sigma_0 \frac{\omega_c\tau}{(\omega_c\tau)^2 - (i + \omega\tau)^2} \tag{3}$$

where $\sigma_0 = e^2 E_F\tau/(\pi\hbar^2)$, τ is the relaxation time (plasmon lifetime), $\omega_c \approx eB_\perp v_F^2/E_F$ is the cyclotron frequency, with $B_\perp$, v_F, and E_F being the external static magnetic field perpendicular onto the graphene surface, the graphene Fermi velocity, and the Fermi energy, respectively.

The surface conductivities in Eqs. 2 and 3 show that graphene under a nonzero static magnetic field is lossy; thus, the eigenvalue problem defining the band structure of graphene metasurfaces becomes non-Hermitian. Therefore, most of the traditional electromagnetic eigenmode solvers are not particularly efficient to compute band diagrams of such metasurfaces. To circumvent this problem, we used the numerical solver of Comsol based on the FEM method to calculate the band diagrams of the graphene metasurfaces investigated in this study. In our full-wave simulations, electric sources are placed at points with low symmetry, so that all modes are excited. Moreover, multiple probe monitors are placed at low-symmetry points, too, to determine the mode frequencies.

In the nonlinear simulations, three nonlinear surface currents are defined in the Comsol software, namely, one for the pump frequency (ν_p), one for the signal frequency (ν_s), and one for the idler frequency (ν_i). These nonlinear currents are coupled via the optical fields of the interacting modes, as described by the following equations

$$J_p^{surf} = 6\sigma_{p,surf}^{(3)} E_s E_i E_p^* \tag{4}$$

$$J_s^{surf} = 3\sigma_{s,surf}^{(3)} E_p E_p E_i^* \tag{5}$$

$$J_i^{surf} = 3\sigma_{i,surf}^{(3)} E_p E_p E_s^* \tag{6}$$

Here, the third-order surface conductivity is defined as $\sigma_{\alpha,surf}^{(3)} = -i\epsilon_0\omega_\alpha h_{eff}\chi^{(3)}$, α = p, s, i, where $\chi^{(3)}$ is the third-order bulk susceptibility and the thickness of graphene is assumed to be $h_{eff} = 0.3$ nm (*25*). Moreover, the electric fields E_α, α = p, s, i, are the amplitudes of the pump, signal, and idler, respectively. More details about the nonlinearity of magnetized graphene and the coupled-mode theory describing the FWM interaction of graphene edge modes can be found in the Supplementary Materials.

SUPPLEMENTARY MATERIALS

Supplementary material for this article is available at http://advances.sciencemag.org/cgi/content/full/6/13/eaaz3910/DC1

Section S1. Optical properties of graphene in an external static magnetic field
Section S1.1. Linear optical properties of graphene
Section S1.2. Nonlinear optical properties of graphene
Section S2. Coupled-mode theory describing the FWM nonlinear process
Section S3. Influence of optical losses on graphene topological plasmonic systems
Section S4. Influence of the substrate on graphene topological plasmonic systems
Fig. S1. Dependence of the effective waveguide nonlinear coefficient γ on *z*.
Fig. S2. Effect of optical losses as described by the coupled-mode theory.
Fig. S3. Band diagrams of a graphene metasurface on a PMMA substrate.
References (*39–45*)

REFERENCES AND NOTES

1. F. D. M. Haldane, S. Raghu, Possible realization of directional optical waveguides in photonic crystals with broken time-reversal symmetry. *Phys. Rev. Lett.* **100**, 013904 (2008).
2. S. Raghu, F. D. M. Haldane, Analogs of quantum-hall-effect edge states in photonic crystals. *Phys. Rev. A* **78**, 033834 (2008).
3. Z. Wang, Y. Chong, J. D. Joannopoulos, M. Soljacic, Observation of unidirectional backscattering-immune topological electromagnetic states. *Nature* **461**, 772–775 (2009).
4. L. Lu, J. D. Joannopoulos, M. Soljacic, Topological photonics. *Nat. Photonics* **8**, 821–829 (2014).

5. L. Lu, J. D. Joannopoulos, M. Soljacic, Topological states in photonic systems. *Nat. Phys.* **12**, 626–629 (2016).

6. A. B. Khanikaev, G. Shvets, Two-dimensional topological photonics. *Nat. Photonics* **11**, 763–773 (2017).

7. C. Liu, W. Gao, B. Yang, S. Zhang, Disorder-induced topological state transition in photonic metamaterials. *Phys. Rev. Lett.* **119**, 183901 (2017).

8. T. Ozawa, H. M. Price, A. Amo, N. Goldman, M. Hafezi, L. Lu, M. Rechtsman, D. Schuster, J. Simon, O. Zilberberg, I. Carusotto, Topological photonics. *Rev. Mod. Phys.* **91**, 015006 (2019).

9. Z. Wang, Y. D. Chong, J. D. Joannopoulos, M. Soljacic, Reflection-free one-way edge modes in a gyromagnetic photonic crystal. *Phys. Rev. Lett.* **100**, 013905 (2008).

10. Y. Yang, Y. Poo, R.-x. Wu, Y. Gu, P. Chen, Experimental demonstration of one-way slow wave in waveguide involving gyromagnetic photonic crystals. *Appl. Phys. Lett.* **102**, 231113 (2013).

11. S. Mittal, J. Fan, S. Faez, A. Migdall, J. M. Taylor, M. Hafezi, Topologically robust transport of photons in a synthetic gauge field. *Phys. Rev. Lett.* **113**, 087403 (2014).

12. D. D. Solnyshkov, O. Bleu, G. Malpuech, Topological optical isolator based on polariton graphene. *Appl. Phys. Lett.* **112**, 031106 (2018).

13. C. He, X.-L. Chen, M.-H. Lu, X.-F. Li, W.-W. Wan, X.-S. Qian, R.-C. Yin, Y.-F. Chen, Tunable one-way cross-waveguide splitter based on gyromagnetic photonic crystal. *Appl. Phys. Lett.* **96**, 111111 (2010).

14. M. Hafezi, S. Mittal, J. Fan, A. Migdall, J. M. Taylor, Imaging topological edge states in silicon photonics. *Nat. Photonics* **7**, 1001–1005 (2013).

15. X. Cheng, C. Jouvaud, X. Ni, S. H. Mousavi, A. Z. Genack, A. B. Khanikaev, Robust reconfigurable electromagnetic pathways within a photonic topological insulator. *Nat. Mater.* **15**, 542–548 (2016).

16. X. Zang, C. Jiang, Edge mode in nonreciprocal photonic crystal waveguide: Manipulating the unidirectional electromagnetic pulse dynamically. *J. Opt. Soc. Am. B* **28**, 554–557 (2011).

17. J.-X. Fu, R.-J. Liu, Z.-Y. Li, Robust one-way modes in gyromagnetic photonic crystal waveguides with different interfaces. *Appl. Phys. Lett.* **97**, 041112 (2010).

18. J.-X. Fu, J. Lian, R.-J. Liu, L. Gan, Z.-Y. Li, Unidirectional channel-drop filter by one-way gyromagnetic photonic crystal waveguides. *Appl. Phys. Lett.* **98**, 211104 (2011).

19. W. Qiu, Z. Wang, M. Soljačić, Broadband circulators based on directional coupling of one-way waveguides. *Opt. Express* **19**, 22248–22257 (2011).

20. B. Bahari, A. Ndao, F. Vallini, A. El Amili, Y. Fainman, B. Kante, Nonreciprocal lasing in topological cavities of arbitrary geometries. *Science* **358**, 636–640 (2017).

21. P. St-Jean, V. Goblot, E. Galopin, A. Lemaître, T. Ozawa, L. Le Gratiet, I. Sagnes, J. Bloch, A. Amo, Lasing in topological edge states of a one-dimensional lattice. *Nat. Photonics* **11**, 651–656 (2017).

22. S. Mittal, E. A. Goldschmidt, M. Hafezi, A topological source of quantum light. *Nature* **561**, 502–506 (2018).

23. S. Kruk, A. Poddubny, D. Smirnova, L. Wang, A. Slobozhanyuk, A. Shorokhov, I. Kravchenko, B. Luther-Davies, Y. Kivshar, Nonlinear light generation in topological nanostructures. *Nat. Nanotechnol.* **14**, 126–130 (2019).

24. D. Smirnova, S. Kruk, D. Leykam, E. Melik-Gaykazyan, D.-Y. Choi, Y. Kivshar, Third-harmonic generation in photonic topological metasurfaces. *Phys. Rev. Lett.* **123**, 103901 (2019).

25. X. Yao, A. Belyanin, Giant optical nonlinearity of graphene in a strong magnetic field. *Phys. Rev. Lett.* **108**, 255503 (2012).

26. D. Jin, T. Christensen, M. Soljačić, N. X. Fang, L. Lu, X. Zhang, Infrared topological plasmons in graphene. *Phys. Rev. Lett.* **118**, 245301 (2017).

27. D. Pan, R. Yu, H. Xu, F. J. Garciá de Abajo, Topologically protected Dirac plasmons in a graphene superlattice. *Nat. Commun.* **8**, 1243 (2017).

28. S. Lavdas, N. C. Panoiu, Theory of pulsed four-wave mixing in one-dimensional silicon photonic crystal slab waveguides. *Phys. Rev. B* **93**, 115435 (2016).

29. M. P. Nielsen, X. Shi, P. Dichtl, S. A. Maier, R. F. Oulton, Giant nonlinear response at a plasmonic nanofocus drives efficient four-wave mixing. *Science* **358**, 1179–1181 (2017).

30. D. Chatzidimitriou, A. Pitilakis, E. E. Kriezis, Rigorous calculation of nonlinear parameters in graphene-comprising waveguides. *J. Appl. Phys.* **118**, 023105 (2015).

31. T. Low, P. Avouris, Graphene plasmonics for terahertz to mid-infrared applications. *ACS Nano* **8**, 1086–1101 (2014).

32. C. R. Dean, A. F. Young, I. Meric, C. Lee, L. Wang, S. Sorgenfrei, K. Watanabe, T. Taniguchi, P. Kim, K. L. Shepard, J. Hone, Boron nitride substrates for high-quality graphene electronics. *Nat. Nanotechnol.* **5**, 722–726 (2010).

33. H. Yan, Z. Li, X. Li, W. Zhu, P. Avouris, F. Xia, Infrared spectroscopy of tunable dirac terahertz magneto-plasmons in graphene. *Nano Lett.* **12**, 3766–3771 (2012).

34. I. Petković, F. I. B. Williams, K. Bennaceur, F. Portier, P. Roche, D. C. Glattli, Carrier drift velocity and edge magnetoplasmons in graphene. *Phys. Rev. Lett.* **110**, 016801 (2013).

35. I. Crassee, J. Levallois, A. L. Walter, M. Ostler, A. Bostwick, E. Rotenberg, T. Seyller, D. Van Der Marel, A. B. Kuzmenko, Giant Faraday rotation in single-and multilayer graphene. *Nat. Phys.* **7**, 48–51 (2011).

36. A. Ferreira, N. M. R. Peres, A. H. Castro Neto, Confined magneto-optical waves in graphene. *Phys. Rev. B* **85**, 205426 (2012).

37. J. W. You, S. R. Bongu, Q. Bao, N. C. Panoiu, Nonlinear optical properties and applications of 2D materials: Theoretical and experimental aspects. *Nanophotonics* **8**, 63–97 (2019).

38. M. Dressel, G. Gruner, *Electrodynamics of Solids: Optical Properties of Electrons in Matter* (Cambridge University Press, 2002).

39. T. Jiang, D. Huang, J. Cheng, X. Fan, Z. Zhang, Y. Shan, Y. Yi, Y. Dai, L. Shi, K. Liu, C. Zeng, J. Zi, J. E. Sipe, Y.-R. Shen, W.-T. Liu, S. Wu, Gate-tunable third-order nonlinear optical response of massless Dirac fermions in graphene. *Nat. Photonics* **12**, 430–436 (2018).

40. E. Hendry, P. J. Hale, J. Moger, A. K. Savchenko, S. A. Mikhailov, Coherent nonlinear optical response of graphene. *Phys. Rev. Lett.* **105**, 097401 (2010).

41. X. Chen, N. C. Panoiu, R. M. Osgood, Theory of Raman-mediated pulsed amplification in silicon-wire waveguides. *IEEE J. Quantum Electron.* **42**, 160–170 (2006).

42. N. C. Panoiu, J. F. McMillan, C. W. Wong, Theoretical analysis of pulse dynamics in silicon photonic crystal wire waveguides. *IEEE J. Sel. Top. Quantum Electron.* **16**, 257–266 (2010).

43. A. W. Snyder, J. D. Love, *Optical Waveguide Theory* (Chapman and Hall, 1983).

44. T. Kamalakis, T. Sphicopoulos, A new formulation of coupled propagation equations in periodic nanophotonic waveguides for the treatment of Kerr-induced nonlinearities. *IEEE J. Quantum Electron.* **43**, 923–933 (2007).

45. D. Michaelis, U. Peschel, C. Wachter, A. Brauer, Reciprocity theorem and perturbation theory for photonic crystal waveguides. *Phys. Rev. E* **68**, 065601 (2003).

Science Advances

Four-wave mixing of topological edge plasmons in graphene metasurfaces

Jian Wei You, Zhihao Lan and Nicolae C. Panoiu

ARTICLE TOOLS	http://advances.sciencemag.org/content/6/13/eaaz3910
SUPPLEMENTARY MATERIALS	http://advances.sciencemag.org/content/suppl/2020/03/23/6.13.eaaz3910.DC1
REFERENCES	This article cites 43 articles, 2 of which you can access for free http://advances.sciencemag.org/content/6/13/eaaz3910#BIBL
PERMISSIONS	http://www.sciencemag.org/help/reprints-and-permissions

Use of this article is subject to the Terms of Service